

Modeling and analysis of high-speed electro-optic modulation in high confinement silicon waveguides using metal-oxide-semiconductor configuration

C. A. Barrios^{a)}

Nanophotonics Technology Center, Universidad Politécnica de Valencia, Valencia 46022, Spain

M. Lipson

School of Electrical and Computer Engineering, Cornell University, Ithaca, New York 14853

(Received 22 June 2004; accepted 16 September 2004)

We analyze the electrical and optical properties of a silicon electro-optic waveguide modulator using a metal-oxide-semiconductor (MOS) configuration. The device performance is studied under different modes of operation of the MOS diode and gate oxide thicknesses. Our calculations indicate that this scheme can be used for achieving high-speed submicron waveguide active devices on silicon on insulator. A microring resonator intensity modulator is predicted to exhibit switching times on the order of tens of picoseconds with modulation depth of 73% by employing a bias voltage of only 5 V. © 2004 American Institute of Physics. [DOI: 10.1063/1.1814791]

I. INTRODUCTION

Silicon as photonic material has remarkable properties. It is transparent in the range of optical telecommunications wavelengths (1.3 μm and 1.55 μm) and has high index of refraction, which allows for the fabrication of high-contrast submicron structures.¹ In addition, the mature Si microelectronics [bipolar or complementary metal-oxide semiconductor] technology enables the implementation of dense silicon-based integrated systems on-chip. Si-on-insulator (SOI) strip waveguide technology has been shown to be an appropriate platform to achieve compact (submicron size) photonic devices.² The use of crystalline Si instead of polysilicon or amorphous Si as the waveguide core reduces scattering and absorption losses.²

Si photonic structures that bend, split, couple, and filter light have recently been demonstrated in silicon,²⁻⁴ but the flow of light in these structures is predetermined by the structure design and cannot be modified. Active (or tunable) waveguide devices are essential elements to control light for information processing (e.g., coding-decoding, routing, multiplexing, timing, logic operations, etc.) in high-density integrated-optic circuits. In these devices, the complex effective refractive index of the structure is varied in order to produce a phase or intensity modulation.

The main methods to alter the refractive index in Si are the thermo-optic effect and the plasma dispersion effect. The thermo-optic effect is rather slow and can be used only up to 1 MHz modulation frequency.⁵ For higher speed, electro-optic devices are required. Unstrained pure crystalline Si does not exhibit linear electro-optic (Pockels) effect and the refractive index changes due to the Franz-Keldysh effect and Kerr effect are very weak. Therefore, the free carrier dispersion effect⁶ is used to change electrically both the real refractive index and optical absorption coefficient.

The free-carrier concentration in Si electro-optic devices

can be varied by injection, accumulation, depletion, or inversion of carriers. *P-i-n* diodes^{7,8} and metal-oxide-semiconductor field-effect-transistors (Refs. 9 and 10) may be employed for this purpose. In a previous work,⁸ we proposed and analyzed a waveguide active structure based on a *p-i-n* diode. That configuration was predicted to provide high modulation depth for very low power consumption. The switching time was calculated to be around 1.29 ns, limited by carrier diffusion (carrier injection process). The use of a MOS diode should lead to higher speed operation since the carrier distribution in the semiconductor is governed by a drift mechanism (electric field).¹¹ Additional advantages of a MOS configuration are negligible dc power consumption and the fact that the refractive index change is localized under the gate electrode, and therefore no carrier confinement methods (such as isolation trenches in a *p-i-n* diode¹²) are necessary. In a MOS structure, however, in carrier depletion, accumulation, or inversion configuration, significant large concentration variations are possible only within small distances (a few tens of nanometers) beneath the insulated gate region.⁹ This produces a small overlap between the optical mode and the nonequilibrium charge distribution in the waveguide, leading to a smaller effective index variation in a MOS system than that in a *p-i-n* configuration. A small index change requires a very long structure, on the order of millimeter, in order to induce a significant modulation depth.¹⁰

In this paper we study a micron-size MOS-based high-index-contrast SOI waveguide for high-speed electro-optic modulation in Si based on strong light confinement. The light confinement enhances the effect of small index changes on the transmission of the device, enabling an ultracompact structure with high modulation depth. In addition, the studied high-index-contrast waveguide structure permits, contrary to previous works, negligible losses for a radius of curvature as small as 5 μm , allowing the implementation of high dense photonic circuits. Section II describes the waveguide structure. Section III presents the electrical and optical models. In Sec. IV, the results from the simulations are presented and

^{a)}Electronic mail: cbarrios@ntc.upv.es

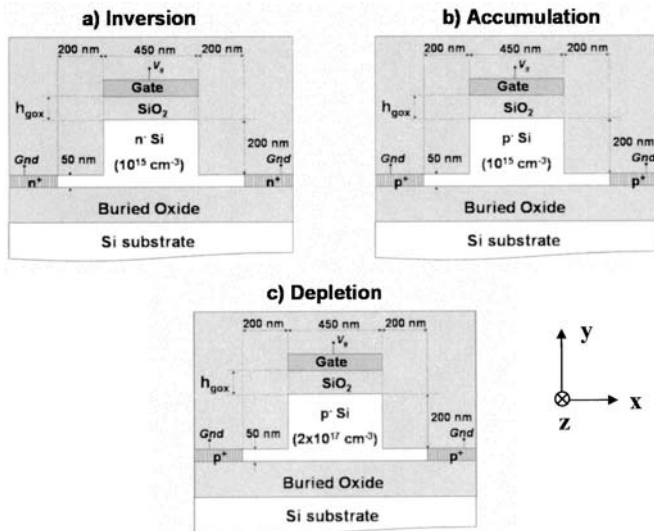


FIG. 1. Schematic cross sections of MOS high-index-contrast SOI rib waveguides for 1.55 μm wavelength. Three doping schemes are shown: (a) for inversion, (b) for accumulation, and (c) for depletion operation.

discussed. In Sec. V, an intensity modulator based on a microring resonator is analyzed. Finally, conclusions are given in Sec. VI.

II. DEVICE DESCRIPTION

Figures 1(a)–1(c) show schematic cross sections of the studied MOS-waveguide configurations. The structures consist of a high aspect ratio [rib height(200 nm) ≫ slab height(50 nm)] rib SOI waveguide with highly doped regions (10^{19} cm^{-3}) defined in the slab at each side of the rib. The structures illustrated in Figs. 1(a)–1(c) operate under different mechanisms for modulation: carrier inversion (hole inversion layer), hole accumulation, and hole depletion operation regimes, respectively. The inversion and accumulation configurations are based on increasing the hole concentration under the gate oxide, whereas the depletion configuration^{13,14} is based on decreasing the hole concentration in the waveguide core. The justification for the use of the hole (instead of electron) distribution in all the three modulation mechanisms is explained in Sec. III A. The silicon layer (device layer) has a background doping concentration of 10^{15} cm^{-3} in Figs. 1(a) (*n* type) and 1(b) (*p* type), whereas a uniform doping concentration of $p = 2 \times 10^{17} \text{ cm}^{-3}$ is considered in Fig. 1(c). We have assumed the rib cross section height and width dimension to be the ones typical of a 1.55 μm wavelength high-index-contrast strip SOI waveguide, that is, 250 nm and 450 nm, respectively, in order to guarantee single mode operation.⁸ The distance of the doped regions to the rib sidewalls is 200 nm.⁸ A 100 nm thick and 450 nm wide *n*-type highly-doped ($8 \times 10^{18} \text{ cm}^{-3}$) poly-Si layer acts as a gate electrode, whereas the lateral highly doped regions operate as ground (Gnd) electrodes. A top SiO₂ cladding layer covers the whole structure.

III. DEVICE MODEL

A. Optical model

We used the beam propagation method (BPM) (Ref. 15) for the calculation of the modal-field profile and optical losses due to carrier absorption in the waveguide. From the values of the electron and hole concentrations at any point of the Si core waveguide (calculated with the electrical model described below), the induced real refractive index and optical absorption coefficient variations (Δn and $\Delta\alpha$, respectively) produced by free-carrier dispersion at a wavelength of 1.55 μm are calculated by using¹⁶

$$\Delta n = \Delta n_e + \Delta n_h = - [8.8 \times 10^{-22} \Delta N + 8.5 \times 10^{-18} (\Delta P)^{0.8}], \quad (1)$$

$$\Delta\alpha = \Delta\alpha_e + \Delta\alpha_h = 8.5 \times 10^{-18} \Delta N + 6.0 \times 10^{-18} \Delta P, \quad (2)$$

where

Δn_e is the refractive index change due to electron concentration change;

Δn_h is the refractive index change due to hole concentration change;

ΔN is the electron concentration change in cm^{-3} ;

ΔP is the hole concentration change in cm^{-3} ;

$\Delta\alpha_e$ (in cm^{-1}) is the absorption coefficient variations due to ΔN ;

$\Delta\alpha_h$ (in cm^{-1}) is the absorption coefficient variation due to ΔP .

Equation (1) indicates that the effect on the refractive index of holes is approximately three times larger than that due to electrons for the same carrier concentration. Equation (2) reveals that the contribution to the absorption coefficient due to holes is lower than that due to electrons. These two facts justify the use of the hole distribution to vary the refractive index for all the MOS modes of operation illustrated in Fig. 1.

B. Electrical model

A two-dimensional (2D) simulation package, ATLAS from SILVACO,¹⁷ was employed to achieve the electrical calculations. The suitability of this device modeling software to analyze electro-optic modulators in SOI waveguides has been demonstrated in other works.^{8,12,18,19} This program simulates internal physics and device characteristics of semiconductor devices by solving Poisson's equation and the charge continuity equations for electrons and holes numerically. The surfaces of the waveguide have been considered oxide passivated. The main parameters used in the simulations are shown in Table I.

IV. RESULTS AND DISCUSSION

Section IV A discusses the modal and geometry characteristics of the waveguide structure. Section IV B analyzes the variation of the effective refractive index and optical losses of the configurations illustrated in Fig. 1 for two gate oxide thicknesses, $h_{\text{gox}} = 100 \text{ nm}$ and $h_{\text{gox}} = 200 \text{ nm}$, as a function of the applied bias under steady-state conditions. In

TABLE I. Main parameters used in the simulations at 300 K.

Si refractive index $n_{\text{Si}}(\lambda=1.55 \mu\text{m})$	3.43
n -type ($8 \times 10^{18} \text{ cm}^{-3}$) poly-Si refractive index ($\lambda=1.55 \mu\text{m}$)	3.41 ^a
SiO_2 refractive index $n_{\text{SiO}_2}(\lambda=1.55 \mu\text{m})$	1.46
n -type ($8 \times 10^{18} \text{ cm}^{-3}$) poly-Si absorption coefficient (dB/cm)	352.4 ^b
Electron carrier lifetime τ_n (ns)	50 ^c
Hole carrier lifetime τ_p (ns)	50 ^c
Si background carrier conc. (cm^{-3})	1×10^{15}

^aFrom Eq. (1).^bFrom Eq. (2) and assuming undoped poly-Si absorption losses of 60 dB/cm (Ref. 10).^cFrom Ref. 20.

Sec. IV C, the dynamic characteristics of the MOS waveguide under different operation regimes are discussed.

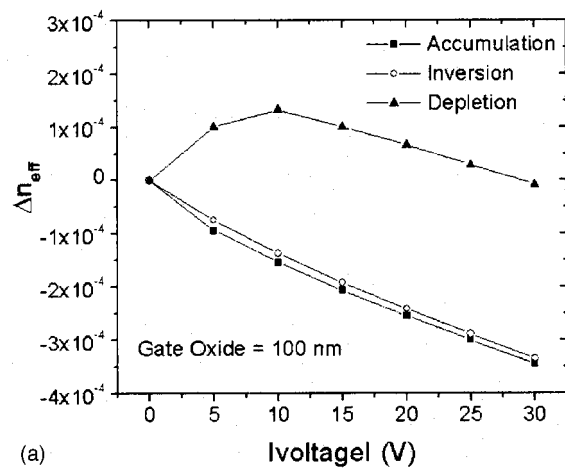
A. Optical characteristics

The geometry of the configurations shown in Fig. 1 is similar to that discussed in Ref. 8. All the structures exhibit single mode operation for both TE-like and TM-like polarization modes and gate oxide thicknesses $h_{\text{gox}}=100 \text{ nm}$ and $h_{\text{gox}}=200 \text{ nm}$. As indicated in Ref. 8, the considered distance of the highly-doped regions to the rib sidewalls (200 nm) and the slab thickness (50 nm) avoid excessive optical losses from the highly-doped regions and enables implementing low-loss bent waveguides with a radius of curvature as small as 5 μm .

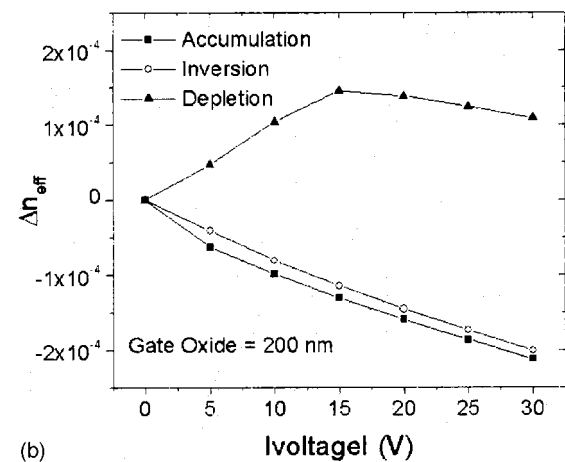
Optical coupling from (to) an optical fiber to (from) the considered high-index-contrast rib waveguide can be efficiently achieved by using an inverse nanotaper as that reported in Ref. 3. In Ref. 3 it is shown that mode delocalization can be used in order to effectively bridge between the mode and index mismatch of index submicron size waveguides and large fibers using compact structures.

B. Static (dc) characteristics

The main difference of the structure studied in this work and that in Ref. 8 is the presence of a gate electrode. This highly-doped region may add significant optical losses if its distance to the Si waveguide (h_{gox}) is too short, since it would overlap significantly with the optical mode field. On the other hand, h_{gox} cannot be very long in order to allow for small operation voltages. Therefore, a tradeoff must be found for the value of h_{gox} . Figures 2(a) and 2(b) show the calculated effective refractive index change Δn_{eff} for the TE-like mode as a function of the absolute value of the gate voltage V_g for $h_{\text{gox}}=100 \text{ nm}$ and $h_{\text{gox}}=200 \text{ nm}$, respectively, for the three MOS operation modes. As expected, higher values of $|\Delta n_{\text{eff}}|$ are obtained for $h_{\text{gox}}=100 \text{ nm}$ under the same operation mode. The bias dependencies of the accumulation- and inversion-mode configurations are similar for both values of h_{gox} . In both cases, a thin layer of holes is formed beneath the gate oxide. The hole concentration in this layer increases with the absolute value of the gate voltage (negative). The values of $|\Delta n_{\text{eff}}|$ are slightly higher for the accumulation mode than for the inversion mode for the same V_g , because holes are majority carriers for the former regime and minor-



(a)



(b)

FIG. 2. Steady-state effective refractive index variation of the TE-like fundamental mode as a function of the absolute voltage of the gate voltage for inversion (squares), accumulation (circles), and depletion (triangles) operation modes for gate oxide thicknesses of (a) $h_{\text{gox}}=100 \text{ nm}$ and (b) $h_{\text{gox}}=200 \text{ nm}$. The applied voltage is negative for the inversion and accumulation modes and positive for the depletion mode.

ity carriers in the latter, and therefore, higher hole concentration values are obtained in the former. In both Figs. 2(a) and 2(b), it is seen for the depletion case that, as the gate voltage increases, Δn_{eff} initially increases due to the increase of the depleted layer region; then Δn_{eff} reaches a maximum at a certain voltage and it decreases as the gate voltage increases. This is because of the formation of an electron inversion layer beneath the gate oxide when the threshold voltage V_t of the MOS diode is exceeded (strong inversion condition). For the configuration of Fig. 1(c), $V_t=7.9 \text{ V}$ and 14.9 V for $h_{\text{gox}}=100 \text{ nm}$ and $h_{\text{gox}}=200 \text{ nm}$, respectively. The increase of carriers (electrons) produces an opposite effect (decrease of n_{eff}) as that induced by the depleted region (increase of n_{eff}), reducing the total effective index variation. The inversion layer formation is illustrated in Fig. 3, which shows the hole and electron two-dimensional distribution in the Si core waveguide for the device of Fig. 1(c), $V_g=20 \text{ V}$ and $h_{\text{gox}}=200 \text{ nm}$.

Figure 4 shows the calculated optical losses for the TE-like mode due to carrier absorption in the semiconductor and

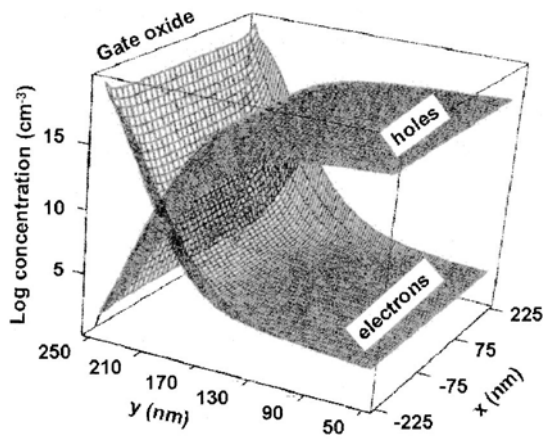


FIG. 3. Steady-state carrier 2D distribution in the Si core waveguide for the depletion-mode operation. The gate voltage is $V_g=20$ V and $h_{gox}=200$ nm. Strong inversion condition is observed (electron inversion layer beneath the gate oxide).

the gate as a function of the gate voltage. The losses for $h_{gox}=100$ nm are considerably higher than those for $h_{gox}=200$ nm. This is because the optical mode overlaps significantly with the gate electrode for $h_{gox}=100$ nm, as shown in Fig. 5(a). Smaller overlap occurs for $h_{gox}=200$ nm [Fig. 5(b)]. It is also observed in Fig. 4 that, for both values of h_{gox} , the losses for the depletion mode configuration are higher than those exhibited by the other two configurations, due to the background doping concentration of the Si waveguide ($2 \times 10^{17} \text{ cm}^{-3}$). One can also see that, as V_g increases, the depletion-mode losses initially decrease (increase of the depletion layer width), reach a minimum (at approximately V_d), and then increase again (strong inversion condition). Note, however, that, as will be seen in the following section, the losses for the depletion case can be different under dynamic operation.

According to these results, under dc operation, the accumulation- or the inversion-mode configurations should be desirable since they exhibit losses as low as 3.6 dB/cm for $V_g=0$ V ($h_{gox}=200$ nm). The simulations discussed so far

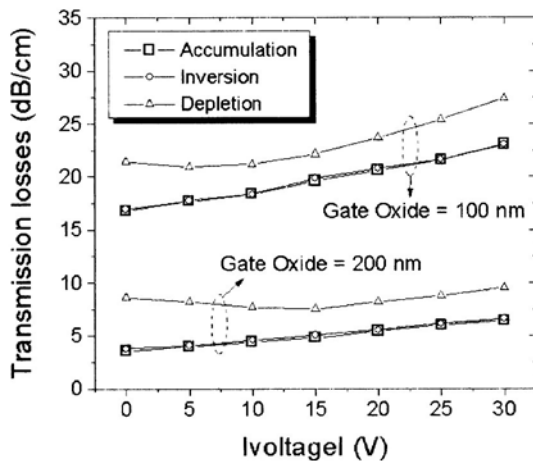


FIG. 4. Optical losses of the TE-like fundamental mode as a function of the absolute value of the gate voltage for inversion (squares), accumulation (circles), and depletion (triangles) operation modes for gate oxide thicknesses of $h_{gox}=100$ nm and $h_{gox}=200$ nm.

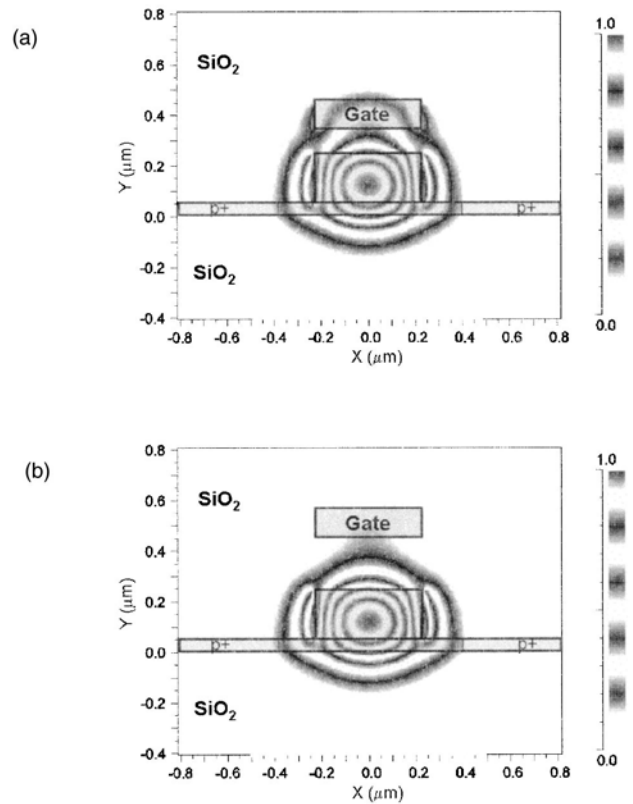


FIG. 5. TE-like fundamental optical mode profile for (a) $h_{gox}=100$ nm and (b) $h_{gox}=200$ nm.

are for TE-like polarization. For the TM-like mode the lower losses achievable are significantly higher, on the order of 20 dB/cm ($h_{gox}=200$ nm); therefore, hereafter we consider only the TE-like fundamental mode for the operation of the device. A gate oxide thickness of 200 nm will be also assumed hereafter in order to avoid excessive losses due to the gate electrode.

C. Dynamic characteristics

1. Small signal response

The small-signal transient response determines the feasibility of the device to be used for high-speed data modulation. In the studied configurations, the small-signal response will be defined by the MOS total capacitance C_T , which is given by the series combination of the gate oxide capacitance C_{gox} and the semiconductor depletion-region capacitance C_d . The value of C_{gox} is constant and corresponds to the maximum capacitance of the system. The value of C_T will depend on the operation mode of the MOS diode.¹¹ Below we discuss the small signal characteristics for the three modes of operation.

(A) In the accumulation regime [Fig. 1(b)], there is no depletion region, therefore $C_T=C_{gox}$. This capacitance remains the same under high frequency operation. For $h_{gox}=200$ nm, we calculated a value of $C_{gox}=10^{-16}$ F/ μm . Thus, assuming a load impedance of $R=50 \Omega$ and $C_T=C_{gox}$, the time constant $\tau_c=RC_T$ of the device results to be 5×10^{-15} s/ μm . For example, for a 20 μm long device $\tau_c=1 \times 10^{-1}$ ps indicating the suitability of this configuration for

high-speed operation. The optical losses will be the same as those calculated in the dc analysis for any operation frequency and gate voltage under the accumulation mode of operation.

(B) For the depletion-mode structure shown in Fig. 1(c), the total capacitance of the system will depend on the operation frequency and bias voltage. At low frequencies and $V_g < V_t$, the total capacitance will be smaller than C_{gox} due to the depletion region capacitance. At low frequencies and $V_g > V_t$ (strong inversion), the formation of the inversion layer makes the total capacitance equal to the gate oxide capacitance, as in the accumulation case. At higher frequencies, C_T will coincide with that at low frequencies for $V_g < V_t$; however, for $V_g > V_t$, the electron (inversion layer) concentration will not be able to follow the ac signal and the depletion region capacitance will lead to smaller C_T , producing a smaller time constant than in the accumulation regime. For example, we calculated $C_T = 9.47 \times 10^{-17}$ F/ μm for $V_g = 20$ V and ac frequency of 1 MHz. This suggests that even higher speed operation can be achieved with the depletion mode than with the accumulation mode. Note that, in this case, since the depletion region width remains constant for $V_g > V_t$ (constant capacitance), the optical losses of the structure will be approximately constant for $V_g > V_t$, and equal to the minimum value obtained in the dc analysis (7.67 dB/cm).

(C) The threshold voltage of the inversion configuration [Fig. 1(a)] was estimated to be -1.42 V. This means that the MOS diode will work mainly under strong inversion conditions. Therefore, due to the aforementioned inability of minority carriers to follow high frequency electrical signals, we can infer that the inversion-mode configuration is not appropriate for high-speed electro-optic modulation.

Thus, for small signal ac operation either the accumulation or the depletion modes could be considered. The former exhibits less loss, while the latter may operate at higher frequency.

2. Large signal response (pulse operation).

A large-signal transient study of the accumulation- and depletion-mode structures was carried out by using ATLAS. A 100 ns long gate voltage pulse with OFF-state gate voltage $V_{g,\text{OFF}} = 0$ V and ON-state gate voltage $V_{g,\text{ON}} < 0$ for accumulation and $V_{g,\text{ON}} > 0$ for depletion, was applied to the simulated device. Rise and fall times of the voltage pulse were equal to 10 ps. Figure 6(a) shows the calculated Δn_{eff} for the accumulation- and depletion-mode configurations under pulse operation as a function of $|V_{g,\text{ON}}|$. The dc operation curve for the depletion mode has been also included for comparison purposes. The variation of Δn_{eff} corresponding to the accumulation is the same for both dc and transient operations. However, a significant Δn_{eff} increase is observed for the depletion case when it is pulse-operated as compared to the dc operation for gate voltages equal or higher than the threshold voltage ($V_t = 14.9$ V). This is because, for those gate voltages, the device is operated under deep depletion conditions:¹¹ the inversion layer is not or only partially formed since the generation of minority carriers cannot keep up with the amount needed to form the inversion layer and,

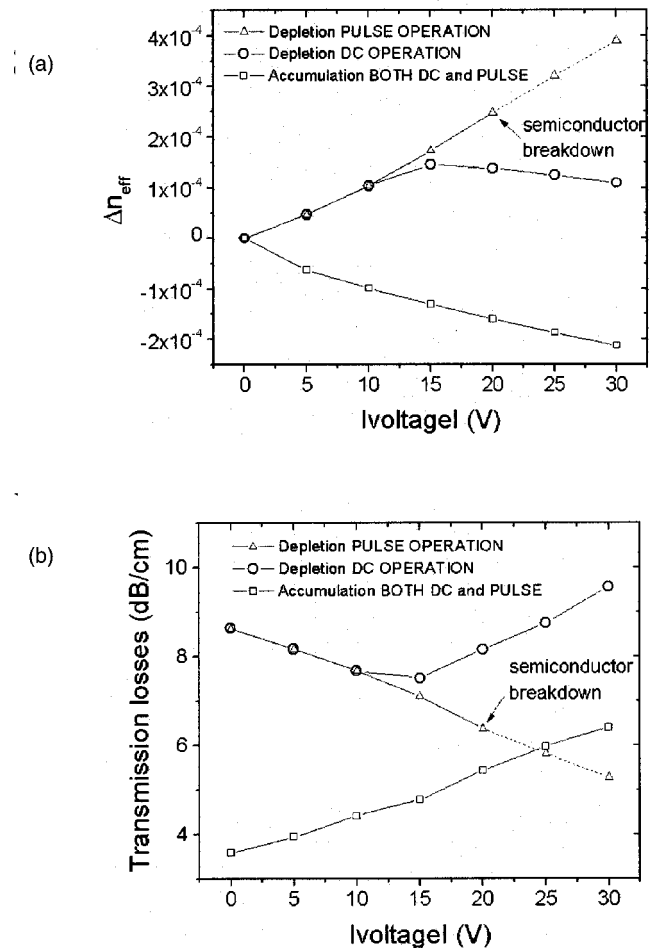


FIG. 6. Effective refractive index variation of the TE-like fundamental mode as a function of the absolute value of the ON-state gate voltage for depletion mode under pulse (triangles) and dc (circles) operation and for the accumulation mode (squares). (b) Optical losses for the same configurations. Dashed lines indicate that the Si breakdown electric field has been exceeded. The gate oxide thickness is $h_{\text{gox}} = 200$ nm. The applied voltage is negative for the accumulation case and positive for the depletion mode.

therefore, the depletion layer can increase beyond its maximum steady-state value, resulting in a capacitance that further decreases with voltage. The rate of change of the gate voltage (pulse ramp slope) required to observe deep depletion is given by²¹

$$\frac{dV_g}{dt} > \frac{qn_i}{2C_{\text{gox}}} \sqrt{\frac{\mu_n V_t}{\tau_n}}, \quad (3)$$

where q is the electron charge, n_i ($\approx 10^{10}$ cm^{-3} at 300 K) is the intrinsic carrier concentration of Si, C_{gox} ($= 2.22 \times 10^{-8}$ F/ cm^2) is the oxide capacitance per unit area, and μ_n ($= 1000$ $\text{cm}^2/\text{V s}$ at 300 K) is the electron mobility. Thus, (dV_g/dt) should be higher than 5.2×10^3 V/s, which is easily accomplished by ramp times employed in high-speed digital signals.

The absence of the inversion layer in the depletion-mode device under pulse operation also leads to a decrease of the transmission losses under deep depletion operation as shown in Fig. 6(b).

It must be mentioned, however, that, for depletion, gate voltages higher than 20 V will lead to an electric field in the

TABLE II. Switching times of the MOS waveguide under accumulation and depletion regimes for different gate voltages. V_g is positive for depletion and negative for accumulation.

$ V_{g,ON} $ (V)	Accumulation		Depletion	
	Turn on (ps)	Turn off (ps)	Turn on (ps)	Turn off (ps)
5	25.5	25.5	10.5	12.7
10	25.5	25.5	12.5	12.7
15	19.1	36.3	14.7	12.2
20	19.1	34.9	14.3	11.9
25	19.1	33.1	15.1	11.6
30	19.1	32.5	16.8	11.3

semiconductor beneath the gate oxide higher than 3×10^5 V/cm, which is the breakdown electric field in Si. This imposes a limitation on the allowed gate voltage (20 V) and, therefore, on the maximum effective refractive index change (2.5×10^{-4}) and minimum transmission losses (6.37 dB/cm) that can be obtained under deep depletion operation.

Table II shows the calculated turn-on and turn-off times of the accumulation and depletion devices for different ON-state gate voltages. The turn-on (turn-off) time is defined as the time needed for the carrier concentration to reach its maximum (minimum) value when the gate voltage is stepped from $V_{g,OFF}(V_{g,ON})$ to $V_{g,ON}(V_{g,OFF})$. Switching times (turn-on time+turn-off time) on the order of tens of picoseconds are predicted, the depletion operation being slightly faster than the accumulation, as expected from the small-signal analysis.

V. ELECTRO-OPTIC MICRORESONATOR MODULATOR

The transmission of an optical resonator is highly sensitive to small index changes, making it ideal for intensity modulation in a short length. Thus, a suitable application of the studied configuration is a waveguide intensity modulator based on a microring resonator as that shown in Fig. 7. R is the radius of the ring and d_g is the spacing between the ring

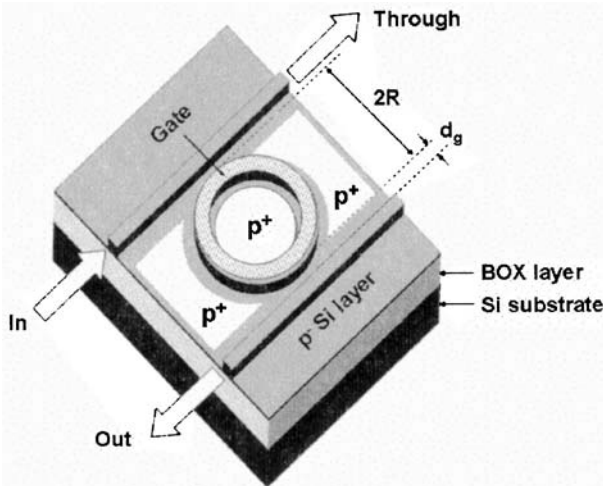


FIG. 7. High-index-contrast waveguide electro-optic modulator based on a microring resonator and a MOS diode. The complex refractive index of the resonant region is changed by applying a bias voltage to the gate electrode.

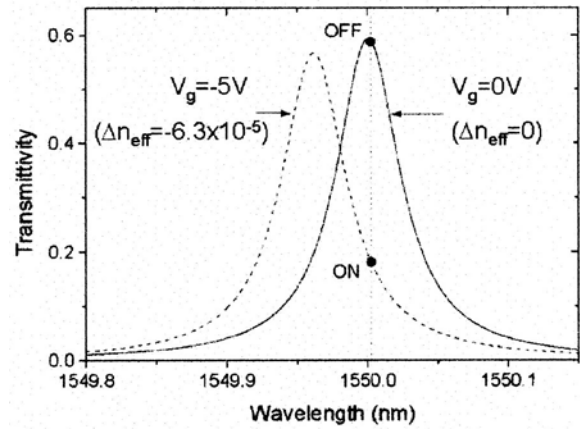


FIG. 8. Spectral transmittance (out port) for the TE-like fundamental optical mode of the simulated electro-optic MOS Si microring modulator (accumulation configuration) for $V_g=0$ V (OFF state) and $V_g=-5$ V ($\Delta n_{eff}=-6.3 \times 10^{-5}$, ON state) for a ring radius of $R=6.9 \mu\text{m}$. The circles illustrate the modulation depth at $\lambda_p=1550.014$ nm.

and a bus waveguide (d_g is the same for both buses). A MOS diode with $h_{gox}=200$ nm is used to change the refractive index in the ring waveguide. The resulting phase change in the ring is converted into an intensity variation at the output port at the operation (probe) wavelength.

We estimated the output transmittivity (out port) of the microring modulator by using the transfer matrix method.²² Bending losses were calculated by employing the BPM,¹⁵ and the spacing between ring and bus waveguides was estimated by using the finite difference time domain method.¹⁵ The ring radius and the power-coupling coefficient ($|\kappa^2|$), which is related to d_g , will determine the main resonator parameters: quality factor Q ($=\omega_0/\Delta\omega_{FWHM}$, with ω_0 the resonance frequency and $\Delta\omega_{FWHM}$ the full frequency width at half maximum), cavity lifetime $\tau_{ph}(=Q/\omega_0)$, and total internal loss A_i [$=(\alpha_T + \alpha_{bend})2\pi R$, with α_T the transmission losses and α_{bend} the bending losses]. For optimum performance, it is required: high Q , for high modulation; small τ_{ph} , for high switching speed; and low A_i , for high transmittance. In order to have a resonance at the probe wavelength $\lambda_{probe}=1550$ nm, the ring radius must also satisfy the condition $2\pi R=m(\lambda_{probe}/2n_{eff})$, where m is an integer and $n_{eff}=n_{eff,OFF}+\Delta n_{eff}$, with $n_{eff,OFF}$ being the effective index in the OFF state ($V_g=0$ V) and Δn_{eff} being the variation of the effective refractive index when a gate voltage is applied (ON state). For the unbiased case, a trade off among the aforementioned ring parameters is found for $R=6.9 \mu\text{m}$ and $|\kappa^2|=0.012$, which corresponds to a gap spacing $d_g=490$ nm. This results, for the accumulation case, in $Q=2.82 \times 10^4$, $\tau_{ph}=23.2$ ps, and $A_i=0.028$ dB ($\alpha_T=3.6$ dB/cm and $\alpha_{bend}=2.9$ dB/cm). For the depletion case, we obtain $Q=2.14 \times 10^4$, $\tau_{ph}=17.6$ ps, and $A_i=0.065$ dB ($\alpha_T=8.6$ dB/cm and $\alpha_{bend}=6.4$ dB/cm). Note that the bending losses are higher for depletion because the refractive index of the core waveguide at zero bias is smaller (due to the background doping of 2×10^{17} cm⁻³) than that of the accumulation case; thus, the index contrast between the Si core and the oxide cladding is reduced, resulting in a weaker optical confinement in the bent waveguide (higher radiation losses)

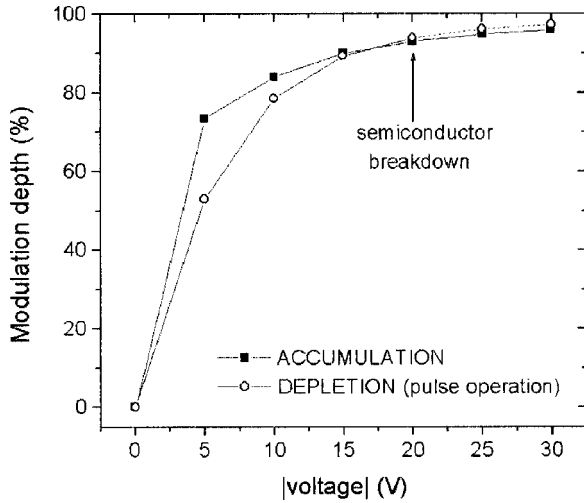


FIG. 9. Calculated modulation depth of the electro-optic MOS microring resonator for the accumulation (squares) and depletion (circles) modes. TE-like fundamental mode is considered. The dashed line indicates that the Si breakdown electric field has been exceeded. The probe wavelengths are 1550.014 nm and 1549.975 nm for the accumulation and depletion cases, respectively. The transmittivity in the OFF state at the corresponding probe wavelength was calculated to be 59% and 23% for the accumulation and depletion cases, respectively.

than that obtained for the accumulation case. It is also seen, that for the same ring parameters, the depletion device exhibits a poorer Q than the accumulation device due to the higher losses (both transmission and bend) in the former.

The value of τ_{ph} for the depletion device is higher than the turn-on and turn-off times due to carrier distribution (Table II), meaning that the switching speed for this configuration will be limited by $\tau_{ph}=17.6$ ps. For the accumulation device, the calculated turn-on and turn-off times due to carrier dynamics (Table II) at low voltage operation (5 V and 10 V) are higher than the photon lifetime of the ring (23.3 ps); therefore, the carrier-induced transient times will limit the switching speed of the ring modulator for the accumulation configuration.

The modulation depth M of the microring modulator at a

given wavelength is defined as $(P_{OFF}-P_{ON})/P_{OFF}$, where P_{OFF} and P_{ON} are the transmitted output power (out port) in the OFF and ON states, respectively. Figure 8 shows the transmission characteristics (output port) for the aforementioned ring parameters ($R=6.9 \mu\text{m}$ and $|\kappa^2|=0.012$) for the accumulation-mode configuration. The refractive index in the cavity is modulated between $V_g=0$ V ($\Delta n=0$, OFF state) and $V_g=-5$ V ($\Delta n=-6.3 \times 10^{-5}$, ON state). The obtained modulation depth and transmittivity at the probe wavelength, 1550.014 nm, are 73.4% and 59%, respectively. We calculated the modulation depth for the accumulation and depletion operation modes as a function of the gate voltage (Fig. 9). Pulse operation (Sec IV C) is assumed for both modes. The probe wavelengths, 1550.014 nm for accumulation and 1549.975 nm for depletion, have been chosen in order to obtain a transmittivity T value of 59% and 23% for the accumulation and depletion modes, respectively, in the OFF state. It is seen that modulation depths higher than 73% can be achieved under the accumulation operation mode for $|V_g| \geq 5$ V. Note that, despite higher values of $|\Delta n_{eff}|$ are obtained under depletion than under accumulation for $|V_g| \geq 10$ V [see Fig. 6(a)], the modulation depth is higher for the latter. This is due to the aforementioned higher losses exhibited by the depletion configuration, which degrades the quality factor of the resonator, and therefore, the achievable modulation depth.

It must be mentioned that, due to the non-negligible value of the thermo-optic effect in Si ($dn/dT \approx 2 \times 10^{-4} \text{K}^{-1}$), temperature effects on the index should be minimized in the studied configurations. This can be achieved by employing strain silicon waveguide²³ introduced in the fabrication process by, for example, controlling the overcladding deposition conditions.²⁴ The introduced strain induces a decrease of the refractive index with temperature, which counterbalances the thermo-optic effect in silicon.²³

For the sake of comparison, Table III shows a list of proposed all-silicon electro-optic modulators recently reported in the literature. The MOS device analyzed in this

TABLE III. All-silicon electro-optic modulators recently proposed in the literature (FCAM = free carrier absorption modulator; M =modulation depth; t_s =switching time).

Year	Author	Electrical structure	Optical structure	M (%)	dc Power (mW)	t_s (ns)	Length (μm)
1997	Cutolo <i>et al.</i> ^a	<i>p-i-n</i>	Bragg reflector	50	4	24.7	3200
1997	Cutolo <i>et al.</i> ^b	BMFET	FCAM	20	126	6	1000
2000	Dainesi <i>et al.</i> ^c	<i>p-i-n</i>	Mach-Zehnder	>90	210	60	1110
2000	Irace <i>et al.</i> ^d	BMFET	<i>Y</i> junction	92	~350	16	5000
2001	Coppola <i>et al.</i> ^e	<i>p-i-n</i>	Bragg reflector	94	0.3	5	3200
2003	Png <i>et al.</i> ^f	<i>p-i-n</i>	Mach-Zehnder	>90	~0.56	0.51	>500
2003	Barrios <i>et al.</i> ^g	<i>p-i-n</i>	Fabry-Perot	80	0.014	1.3	10
2004	Liu <i>et al.</i> ^h	MOS	Mach-Zehnder	97.5	~0.0	~0.6	10 000
2004	Our device	MOS	Ring resonator	73	~0.0	0.051	14

^aReference 25.

^bReference 26.

^cReference 27.

^dReference 28.

^eReference 29.

^fReference 30.

^gReference 8.

^hReference 10.

work is expected to improve significantly previous designs in terms of switching time and dc power consumption

VI. CONCLUSIONS

We have studied an electro-optic MOS SOI high-index-contrast waveguide modulator for 1.55 μm operation wavelength. The real refractive index and absorption coefficient of the core Si waveguide are changed by using the free-carrier dispersion effect produced by a MOS diode. A gate oxide thickness of 200 nm has been shown to be a good tradeoff between low gate electrode losses and low bias voltage operation. Both accumulation and depletion operation modes are well suited for high-speed applications, with the former mode exhibiting lower loss. Modulation depths of 73% and switching times on the order of tens of picoseconds are predicted for a 14 μm diameter microring MOS modulator by using a bias voltage of only 5 V. The studied electro-optic modulator is, therefore, a very promising candidate for implementing Si microphotonic and nanophotonic integrated circuits for high-speed applications.

ACKNOWLEDGMENTS

The authors acknowledge V. Almeida and A. Vonsovici for useful discussion, and support by the National Science Foundation (NSF) under Contract No. ECS-0300387. This work was partially carried out as part of the Interconnect Focus Center Research Program at Cornell University, supported in part by the Microelectronics Advanced Research Corporation (MARCO), its participating companies, and DARPA under Contract No. 2003-IT-674. C. A. B. acknowledges support from the Spanish Ministry of Science and Technology under program "Ramón y Cajal."

¹L. C. Kimerling, *Electrochem. Soc. Interface* **9**(2), 28 (2000).

²K. K. Lee, Ph.D thesis, Massachusetts Institute of Technology, 2001.

³V. A. Almeida, R. Panepucci, and M. Lipson, *Opt. Lett.* **28**, 1302 (2003).

⁴B. E. Little *et al.*, *IEEE Photonics Technol. Lett.* **10**, 549 (1998).

⁵C. Cocorullo, M. Iodice, I. Rendina, and P. M. Sarro, *IEEE Photonics Technol. Lett.* **7**, 363 (1995).

⁶R. A. Soref and B. R. Bennett, *IEEE J. Quantum Electron.* **23**, 123 (1987).

⁷C. Z. Zhao, E. K. Liu, G. Z. Li, Y. Gao, and C. S. Guo, *Opt. Lett.* **21**, 1664 (1996).

⁸C. Angulo Barrios, V. R. Almeida, R. Panepucci, and M. Lipson *J. Lightwave Technol.* **21**, 2332 (2003).

⁹S. R. Giguere, L. Friedman, R. A. Soref, and J. P. Lorenzo, *J. Appl. Phys.* **68**, 4964 (1990).

¹⁰A. Liu, R. Jones, L. Liao, D. Samara-Rubio, D. Rubin, O. Cohen, R. Nicolaescu, and M. Paniccia, *Nature (London)* **427**, 615 (2004).

¹¹S. M. Sze, *Physics of Semiconductor Devices*, 2nd ed. (Wiley, New York, 1981).

¹²C. Angulo Barrios, V. R. Almeida, and M. Lipson, *J. Lightwave Technol.* **21**, 1089 (2003).

¹³J. P. Lorenzo and R. A. Soref, U.S. Patent No. 4,877,299 (31 October 1989).

¹⁴R. A. Soref and L. Friedman, *Int. J. Optoelectron.* **9**, 205 (1994).

¹⁵<http://www.rsoftinc.com/fullwave.htm>

¹⁶R. A. Soref and B. R. Bennett, *SPIE Integr. Opt. Circuit Eng.* **704**, 32 (1987).

¹⁷SILVACO International, 4701 Patrick Henry Drive, Bldg. 1, Santa Clara, CA 94054.

¹⁸P. D. Hewitt and G. T. Reed, *J. Lightwave Technol.* **19**, 387 (2001).

¹⁹P. D. Hewitt and G. T. Reed, *J. Lightwave Technol.* **18**, 443 (2000).

²⁰T. Ernst, A. Vandooren, S. Cristoloveanu, J.-P. Colinge, and D. Flandre, *IEEE Electron Device Lett.* **20**, 209 (1999).

²¹Van Zeghbroeck and J. Bart, *Principles of Semiconductor Devices* (University of Colorado, Boulder, 1999), <http://ece-www.colorado.edu/~bart/book/>

²²A. Yariv, *Electron. Lett.* **36**, 321 (2000).

²³S. M. Weiss, M. Molinari, and P. M. Fauchet, *Appl. Phys. Lett.* **83**, 1980 (2003)

²⁴P. Cheben, D.-X. Xu, S. Janz, and A. Delâge, *Proc. SPIE-Int. Soc. Opt. Eng.* **5117**, 147 (2003).

²⁵A. Cutolo, M. Iodice, A. Irace, P. Spirito, and L. Zeni, *Appl. Phys. Lett.* **71**, 199 (1997).

²⁶A. Cutolo, M. Iodice, P. Spirito, and L. Zeni, *J. Lightwave Technol.* **15**, 505 (1997).

²⁷P. Dainesi *et al.*, *IEEE Photonics Technol. Lett.* **12**, 660 (2000).

²⁸A. Irace, G. Coppola, G. Breglio, and A. Cutolo, *IEEE J. Sel. Top. Quantum Electron.* **6**, 14 (2000).

²⁹G. Coppola, A. Irace, M. Iodice, and A. Cutolo, *Opt. Eng.* **40**, 1076 (2001).

³⁰E. P. Ching, G. T. Reed, R. M. Atta, G. J. Ensell, and A. G. R. Evans, *Proc. SPIE- Int. Soc. Opt. Eng.* **4997**, 190 (2003).